Hindawi
Advances in Materials Science and Engineering
Volume 2020, Article ID 5716548, 14 pages
https://doi.org/10.1155/2020/5716548

Research Article

Constitutive Relationship for Hot Deformation of TB18 Titanium Alloy

Qiang Fu,[1] **Wuhua Yuan**,[1] **and Wei Xiang**[2]

[1]*College of Materials Science and Engineering, Hunan University, Changsha 410082, China*
[2]*Deyang Wanhang Die Forging Co., Ltd., China National Erzhong Group Co., Deyang 618013, China*

Correspondence should be addressed to Wuhua Yuan; yuan46302@163.com

Received 14 March 2020; Revised 7 May 2020; Accepted 16 May 2020; Published 17 June 2020

Academic Editor: Simo-Pekka Hannula

In the present work, the hot deformation behavior of TB18 titanium alloy was investigated by isothermal hot compression tests with temperatures from 650 to 880°C and strain rates from 0.001 to 10 s^{-1}. The flow curves after friction and temperature correction show that the peak stress decreased with the temperature increase and the strain rate decrease. Three typical characteristics of flow behavior indicate the dynamic softening behavior during hot deformation. At a strain rate of 0.001~0.01 s^{-1}, the flow stress continues to decrease as the strain rate increases after the flow stress reaches the peak stress; the flow softening mechanism is dynamic recovery and dynamic recrystallization at a lower temperature and dynamic recrystallization at a higher temperature. The discontinuous yielding phenomenon could be seen at a strain rate of 1 s^{-1}, dynamic recrystallization took place in the β single-phase zone, and flow localization bands were observed in the $\alpha+\beta$ two-phase zone. At a higher strain rate of 10 s^{-1}, the flow instabilities were referred to as the occurrence of flow localization by adiabatic heat. Constitutive equation considering the compensation of strain was also established, and the results show high accuracy to predict the flow stress with the correlation coefficient of 99.2% and the AARE of 6.1%, respectively.

1. Introduction

Owing to the high specific strength, remarkable fracture toughness, excellent creep and corrosion resistance, β titanium alloys have been used widely in many fields such as aerospace, aircraft, ship, and nuclear energy [1–4]. For instance, Ti-10V-2Fe-3Al was used in landing gear forgings in Boeing 777 [5], and landing gear forgings were manufactured by Ti-5Al-5Mo-5V-3Cr-0.5Fe alloys in Boeing-787 and Airbus-350 [6]. Thermomechanical processing to fabricate these large products is very complicated and the key processes are related to two steps as follows: (1) to produce usable and intricate shapes through hot die forging; (2) to meet the high quality mechanical properties through the subsequent heat treatment [7]. Due to the hexagonal close-packed structure (HCP) with less slip systems, titanium alloys are more difficult to deform than other metallic materials, such as Fe alloys [8] and aluminium alloys [9]. Previous studies proved that β titanium alloys had a relatively narrow process window and were sensitive to the processing parameters, such as temperature, strain, and strain rate [7, 10–12]. Finite element simulation has been widely applied in the production of large forgings, and accurate material models are essential to improve the precision of the simulation results.

Considerable research studies have been carried out on the constitutive relationship and flow behavior for the high-temperature deformation by using simulative laboratory tests. Lin et al. [13] studied the flow behavior of TC18 titanium alloy in the $\alpha+\beta$ phase zone by hot compression tests with the strain rates of 0.001–0.1 s^{-1} and temperature of 1033–1123K. Three constitutive models, including the strain-compensated Arrhenius type, Hensel–Spittel (HS), and artificial neural network (ANN) models were used to describe the flow behavior. Long et al. [14] investigated the flow behavior of Ti-6Cr-5Mo-5V-4Al and compared the prediction accuracy between the genetic algorithm optimized Arrhenius model (GAOAM) and the strain-

compensated Arrhenius model (SCAM). Also, dynamic globularization behavior was conducted to explain the flow softening at different strain rates. Zhao et al. [15] considered that the main dynamic restoration mechanism of Ti-10V-2Fe-3Al deformed above β transus temperature is dynamic recovery. Chuan and Liang [16] studied the hot deformation and dynamic recrystallization of Ti-55531 in the β single-phase region, discontinuous yield and flow softening phenomena in the true stress-true strain curves have shown the sensitivity to temperature and strain. Fan et al. [17] found that Ti-7333 exhibits flow instabilities in the form of flow localization when strain rates reach more than $1\,s^{-1}$ and moderate-low strain rate at a lower temperature. Lei et al. [18] indicated that the hot workability of Ti-5Al4Zr8Mo7V is better at higher deformation temperature, higher strain, and lower strain rate.

It is well known that the Arrhenius equation is most widely used to describe the relationship between temperature, stress rate, and flow stress [19–21]. However, it is found that the effect of strain was not considered on the flow stress. In order to accurately predict the flow behavior, the strain-compensated Arrhenius-type constitutive model was proposed [22]. The material constants values of Q, A, n, and α were expressed as different order polynomial functions of strain. The modified models, verified in steels [23], titanium alloys [24], aluminium alloys [25], and magnesium alloys [26], are in good agreement with the experimented flow stress.

TB18 titanium alloy is a new near beta titanium alloy that has potential applications in aerospace structural parts and whose hot workability deserves to be figured out. In the present work, isothermal hot compression tests were conducted under the temperature from 650 to 880°C with a strain rate from 0.001 to $10\,s^{-1}$ to study the hot deformation behavior of TB18, and the strain-compensated Arrhenius-type constitutive model was built to describe the relationship of the flow stress, strain rate, and temperature after the friction and temperature correction. Finally, the flow of softening behavior was analysed. The research results are expected to provide guidance for the application of the alloy.

2. Materials and Methods

The nominal composition of TB18 titanium alloy used in this paper is as follows: (Bal.)Ti, (5.5–6.5%)Cr, (4.5~5.5%)Mo, (4.5~5.5%)V, (3.5~4.5%)Al, and (0.5~1.5%)Nb. The β transus temperature measured using the metallographic method is 798°C. The microstructure of the as-received material is shown in Figure 1, which consists of equiaxed and acicular α phase in the β matrix and grain boundary.

Cylindrical specimens with a size of $\varphi 10 \times 15$ mm were machined from the as-received billet. Hot compression experiments were carried out on a Gleeble 3800 machine with the deformation temperatures of 650, 700, 750, 800, 820, 850, and 880°C, strain rates of 0.001, 0.01, 0.1, 1, and $10\,s^{-1}$, and the height reductions of 60%. A K-type thermocouple with a precision of ±2°C was welded in the middle of the samples to record temperature changes during deformation. All the specimens were heated up to the deformation temperature with 5°C/s and kept for 3 min to homogenize the temperature. Graphite pieces as a lubricant were covered on the two ends of specimens to reduce the friction between specimens and the anvils.

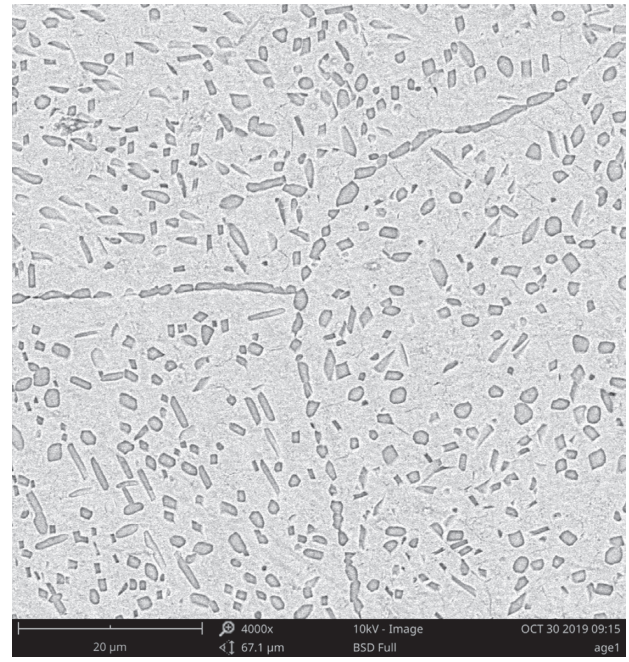

Figure 1: The original microstructure of the as-received alloy.

3. Results and Discussion

3.1. Analysis of True Stress-Strain Curve

3.1.1. Friction Correction. The friction between the specimen and anvils will restrict the metal flow during the deformation, although lubricants were used [27]. The velocity of metal flow gradually increases from the surface to the core with the increase of the deformation, resulting in a barrelled shape of the specimen, as shown in Figure 2. Therefore, the original flow stress should be corrected with friction. A barrelling coefficient was proposed to revise the effect of friction by Roebuck et al. [28], which can be expressed as follows:

$$B = \frac{hR_M^2}{h_0 R_0^2}, \tag{1}$$

where B is the barrelling coefficient, h_0 and h are the height of specimen before and after deformation, R_0 is the initial radius, and R_M is the maximum radius of the specimen after deformation, respectively. When $1 < B \leq 1.1$, there is no need to revise the differences between the original flow stress and the true flow stress; when $B \geq 1.1$, the original flow stress curves must be corrected.

The calculated values of B at different deformation conditions are listed in Table 1. It can be seen that almost all the B values are above 1.1, which means that the original flow stress should be corrected under all the deformation conditions.

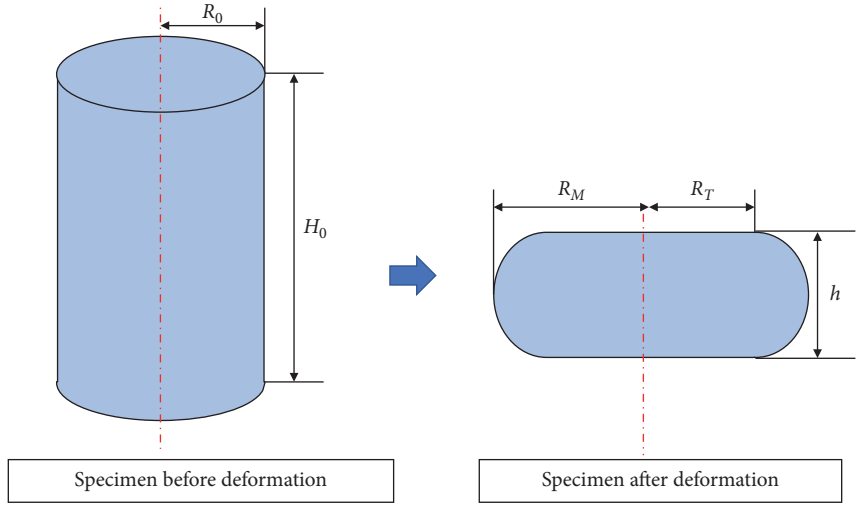

Figure 2: Schematic diagram of the specimen before and after the compression.

Table 1: The barrelling coefficient B values under different deformation conditions.

Strain rate	Deformation temperature (°C)						
	650	700	750	800	820	850	880
0.001	1.19205	1.15483	1.14460	1.14949	1.12273	1.14120	1.09103
0.01	1.20623	1.17324	1.14540	1.14240	1.12167	1.16406	1.13168
0.1	1.25331	1.16809	1.15232	1.16827	1.11149	1.15791	1.14637
1	1.23472	1.18423	1.20384	1.20712	1.12823	1.20444	1.14137
10	1.31615	1.18826	1.21172	1.18175	1.13728	1.20282	1.11533

According to the upper-bound theory [29], the friction-corrected flow stress can be written as follows:

$$\frac{P}{\sigma} = \frac{8bR}{H} \cdot \left\{ \left[\frac{1}{12} + \left(\frac{H}{Rb} \right)^2 \right]^{3/2} - \left(\frac{H}{Rb} \right)^3 - \frac{me^{-b/2}}{24\sqrt{3\left(e^{-b/2} - 1\right)}} \right\}, \tag{2}$$

where P and σ represent the true stress before and after correction, b is the barrel parameter, m is the coefficient of friction, $R = R_0\exp(-\varepsilon/2)$, and $H = h_0\exp(-\varepsilon)$. m and b can be calculated by the following equations:

$$m = \frac{R_f}{h} \times \frac{3\sqrt{3}b}{12 - 2b}, \tag{3}$$

$$b = 4 \times \frac{R_M - R_T}{R_f} \times \frac{h}{h_0 - h}. \tag{4}$$

R_f is the average radius of the specimen after deformation, R_T is the top radius of deformed samples, and R_f and R_T can be calculated by the following:

$$R_f = R_0\sqrt{\frac{h_0}{h}}, \tag{5}$$

$$R_T = \sqrt{3 \times \frac{h_0}{h} \times R_0^2 - 2R_M^2}. \tag{6}$$

Based on equation (2) to equation (6), the flow stress curves after friction correction are shown in Figure 3. It is obvious that the influence of friction between the specimen and the anvils is noteworthy with the increasing strain rate and the decreasing deformation temperature.

3.1.2. Temperature Correction. Adiabatic heating is a common characteristic of stress-strain curves at high temperatures caused by the deformation heat or (and) phase transition. In the compression tests, the welded thermocouple is often not sensitive enough to measure the temperature and record the value by computer [30]. Figure 4 shows the instantaneous temperature recorded by thermocouple during deformation. It can be seen that at strain rates $<1\ s^{-1}$, the instantaneous temperature is almost the same as the setting value, in this situation, deformation heat is usually very small and is transmitted away with plenty of time, so the temperature corrections are not necessary to perform at lower strain rate levels; at strain rates $\geq 1\ s^{-1}$, the instantaneous temperature increases fast as the deformation proceeds, and the value is much bigger than the setting one, the deformation heat could not be transferred from the core to the surface because of short deformation time and low thermal conductivity of titanium alloys. Thus, the flow stress data must be corrected for adiabatic heating. The temperature increase due to deformation heating may be calculated using the following equation [31]:

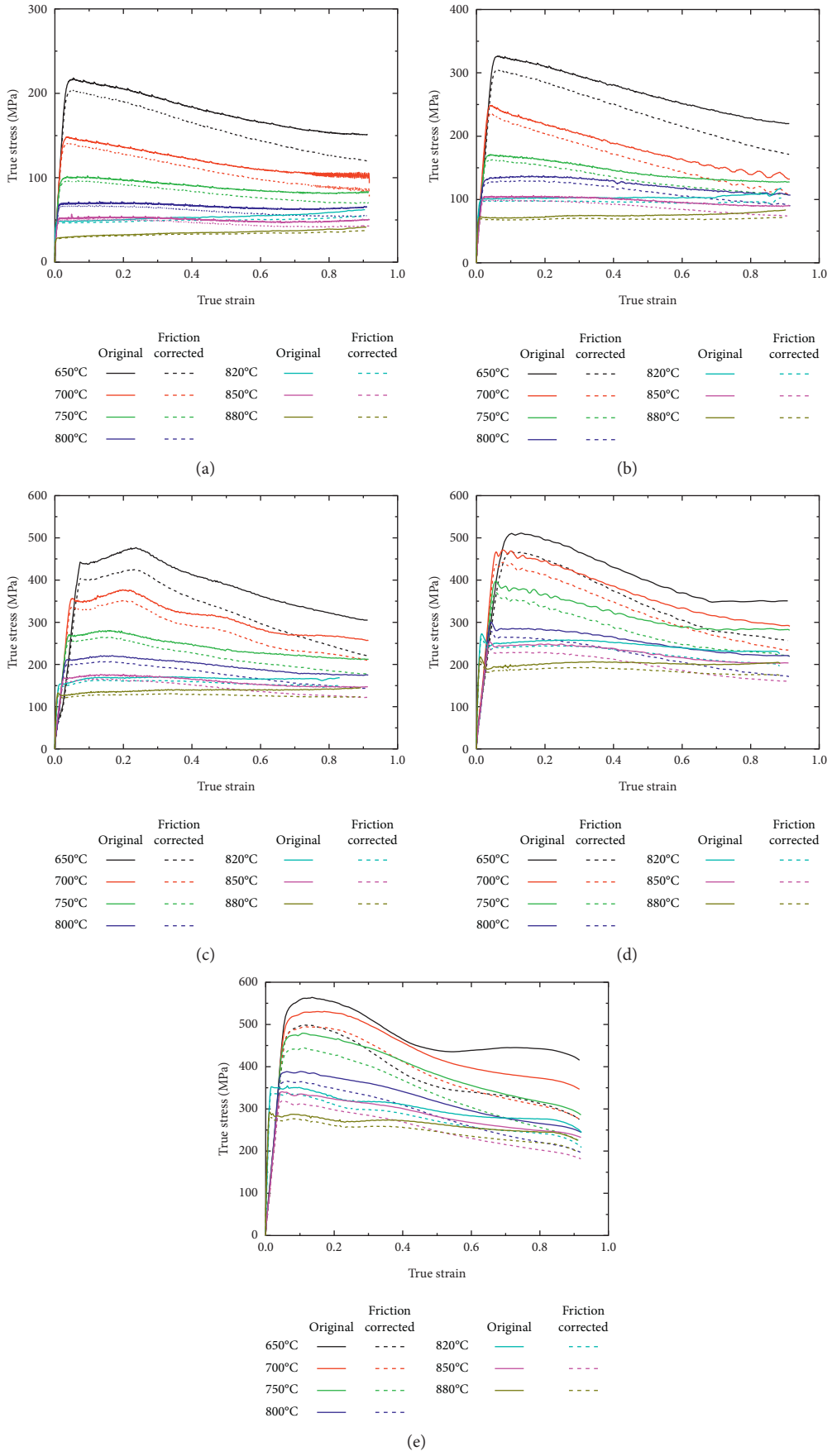

Figure 3: Comparisons between the friction-corrected and original flow stress: (a) 0.001 s^{-1}, (b) 0.01 s^{-1}, (c) 0.1 s^{-1}, (d) 1 s^{-1}, and (e) 10 s^{-1}.

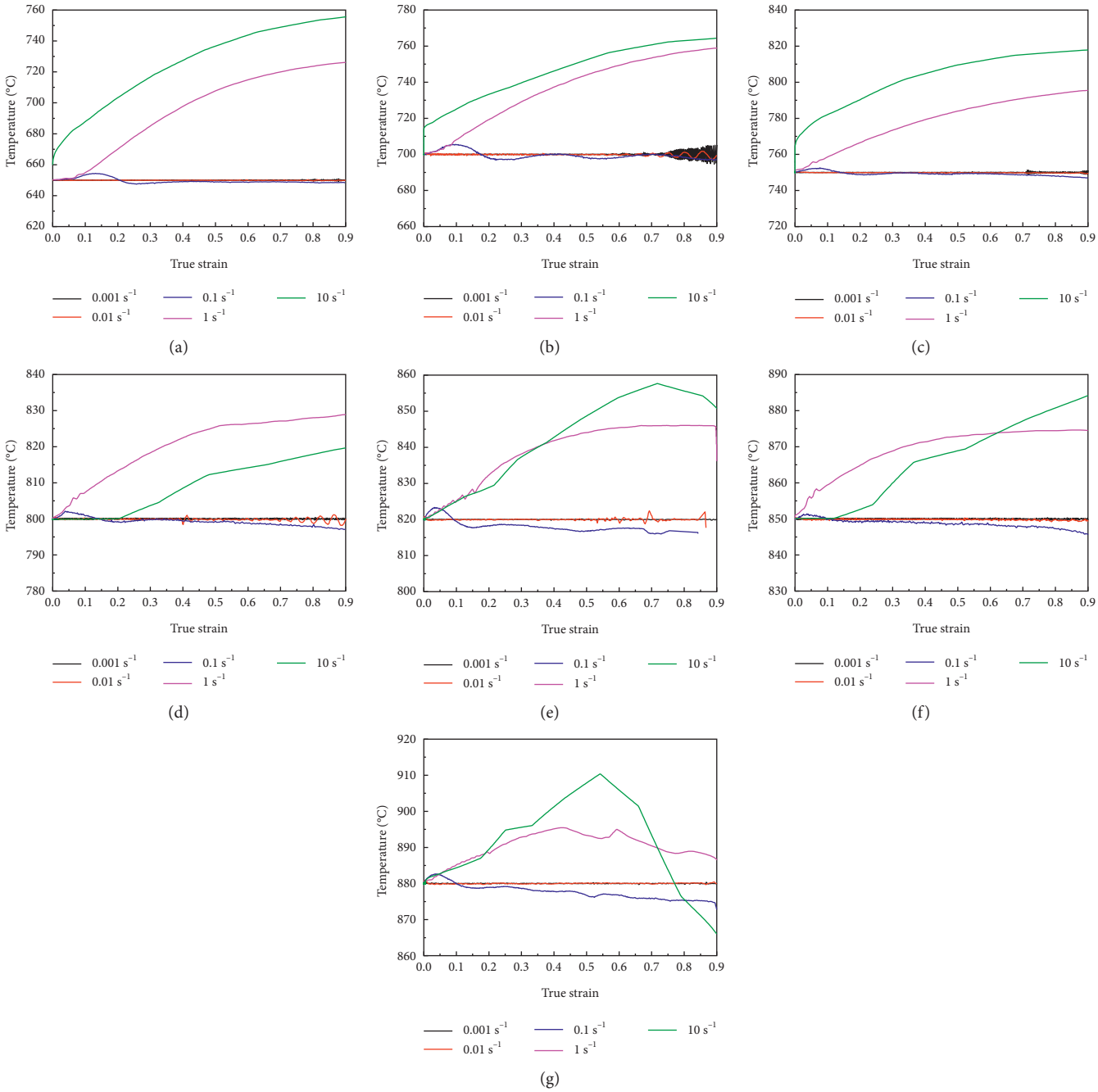

FIGURE 4: Instantaneous temperature of TB18 alloy deformed at different temperatures: (a) 650°C, (b) 700°C, (c) 750°C, (d) 800°C, (e) 820°C, (f) 850°C, and (g) 880°C.

$$\Delta T = \frac{0.95\eta \int_0^{\varepsilon} \sigma d\varepsilon}{\rho C_p}, \tag{7}$$

where ΔT is the variation in temperature, η is the adiabatic correction factor, $\int_0^{\varepsilon} \sigma d\varepsilon$ equals to the area under the true stress-strain curve, and ρ and C_p are the density and the specific heat, respectively. The value of 0.95 is the fraction of mechanical work transformed to heat. The adiabatic correction factor η varies with strain rate: at strain rates $\leq 10^{-3}\,s^{-1}$, $\eta = 0$; at strain rates of $1\,s^{-1}$, $\eta = 0.75$; ad at strain rates $\geq 10\,s^{-1}$, $\eta = 1$ [32, 33].

Figure 5 shows the calculated temperature changes during the compression test from 650°C to 880°C at strain rates of 1 and $10\,s^{-1}$. As can be seen, a linear relationship is shown between true strain and temperature rise, where adiabatic heating is getting higher with the strain increases. When deformed at 650°C with the strain rate of $10\,s^{-1}$ and the true strain of 0.9, the temperature increases by about 90°C.

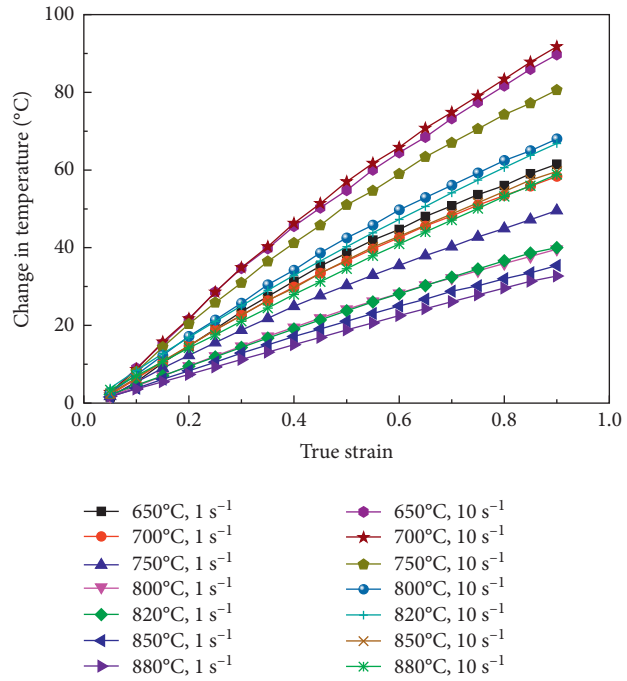

Figure 5: Calculated temperatures variation at stain rates of 1 s^{-1} and 10 s^{-1}.

The measured flow stress curves corrected at strain rates of 1 and 10 s^{-1} takes one of the following forms [34–36]:

$$\dot{\varepsilon} = A_1 \sigma^{n_1} \exp\left(-\frac{Q}{RT}\right) \text{(for low stress level)}, \quad (8)$$

$$\dot{\varepsilon} = A_2 \exp(\beta\sigma) \exp\left(-\frac{Q}{RT}\right) \text{(for high stress level)}, \quad (9)$$

$$\dot{\varepsilon} = A[\sinh(\alpha\sigma)]^n \exp\left(-\frac{Q}{RT}\right) \text{(for all stress levels)}, \quad (10)$$

where Q is the activation energy (kJ/mol), R is the universal gas constant (8.314 J/mol K), $\dot{\varepsilon}$ is the strain rate, T is the deformation temperature (K), and A_1, A_2, A, β, n_1, n, and α are material constants, $\alpha = \beta/n_1$.

The flow stress can be corrected using equations (8) and (9) for low stresses and high stresses, respectively. The correction of flow stress for deformation heating was accomplished by plotting $\ln(\sigma)$ against $1000/T$ at a lower strain rate of 1 s^{-1}, and σ against $1000/T$ at a higher strain rate of 10 s^{-1}, as shown in Figures 6 and 7, respectively; then, the corrected flow stress was calculated by extrapolating back to the preset testing temperatures. Because there is no correlation of flow stress with strain in equations (8) and (9), the correction has to be made for each selected strain value [30, 37].

3.1.3. Flow Behavior Analysis. The true stress-strain curves of TB18 alloy after friction and temperature correction at different experimental conditions are shown in Figures 3 and 8, respectively. It is evident that the flow behaviors are significantly sensitive to deformation temperature and strain

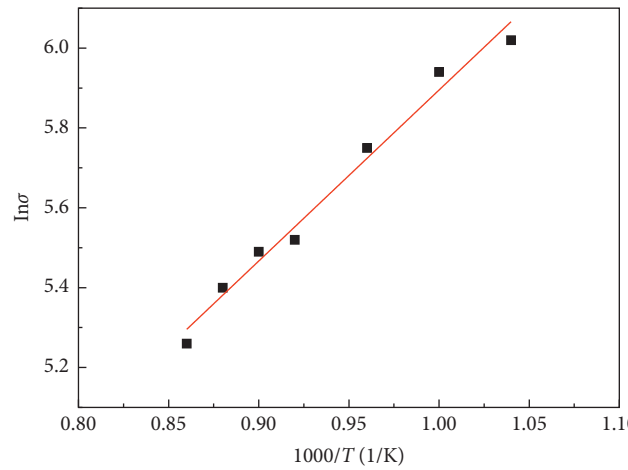

Figure 6: Plot of $\ln(\sigma)$-$1000/T$ at a strain of 0.3 and strain rates of 1 s^{-1}.

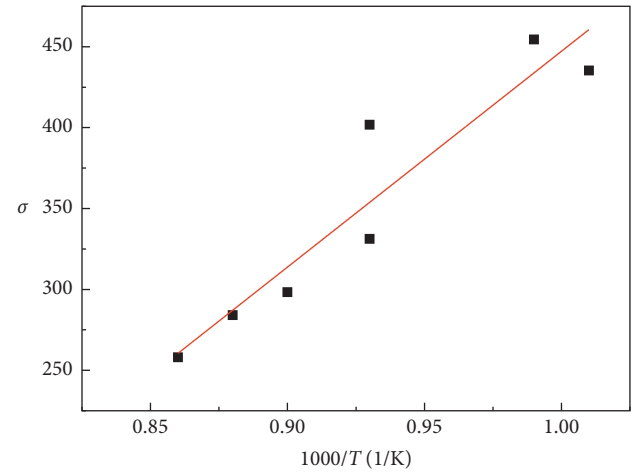

Figure 7: Plot of σ-$1000/T$ at a strain of 0.3 and strain rates of 10 s^{-1}.

rate. At the beginning of deformation, the flow stress increased rapidly to a peak value with increased strain rate, then dynamic softening started, and the flow stress decreases with the decrease of strain rate and the increase of deformation temperature. Figure 9 shows the relationship between peak stress and deformation temperature at different strain rates. The peak stress decreases as the deformation temperature increases while the strain rate declines. The flow softening is significant when deformed at a lower temperature in the $\alpha + \beta$ phase zone and relatively gentle in the β single-phase zone.

The flow curves, reflecting the competition of work hardening and dynamic softening effect, exhibit three typical characteristics at different deformation temperatures and strain rates:

(1) At a strain rate of 0.001~0.01 s^{-1} with a deformation temperature of 650~880°C, as shown in Figures 3(a) and 3(b), the flow stress continues to decrease as the strain increases after the flow stress reaches the peak

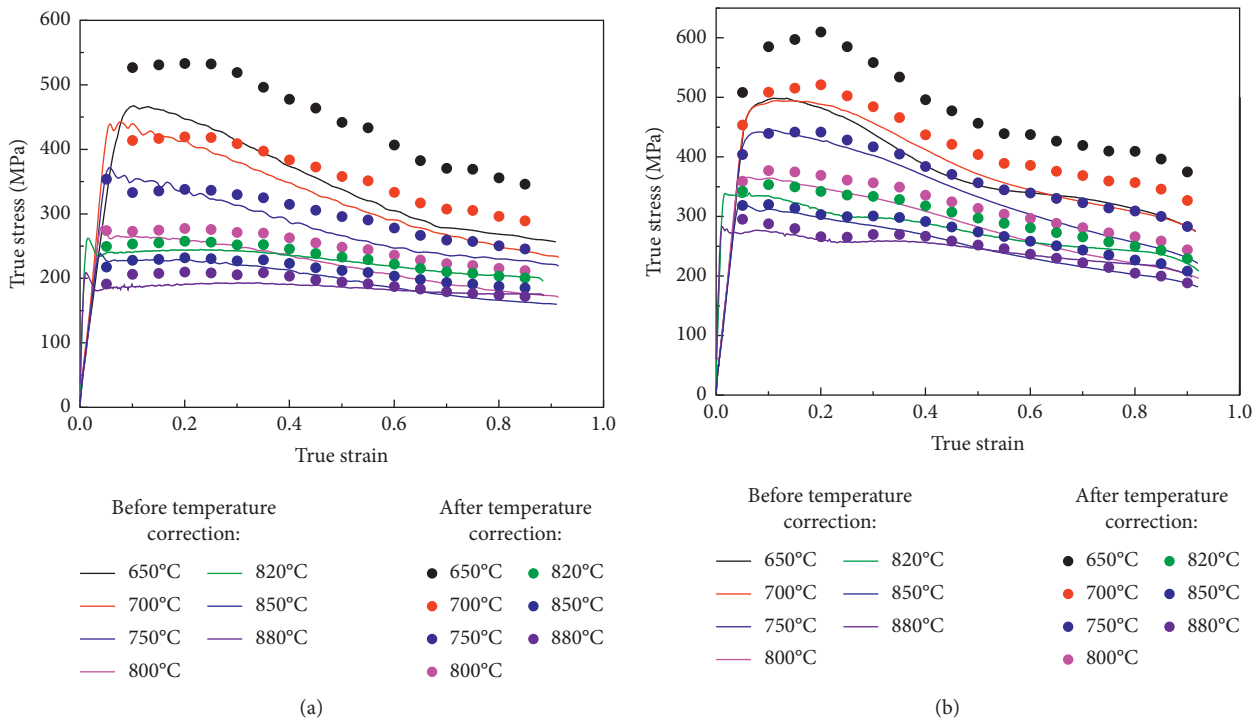

Figure 8: Flow curves of TB18 before and after temperature correction: (a) $1\,s^{-1}$ and (b) $10\,s^{-1}$.

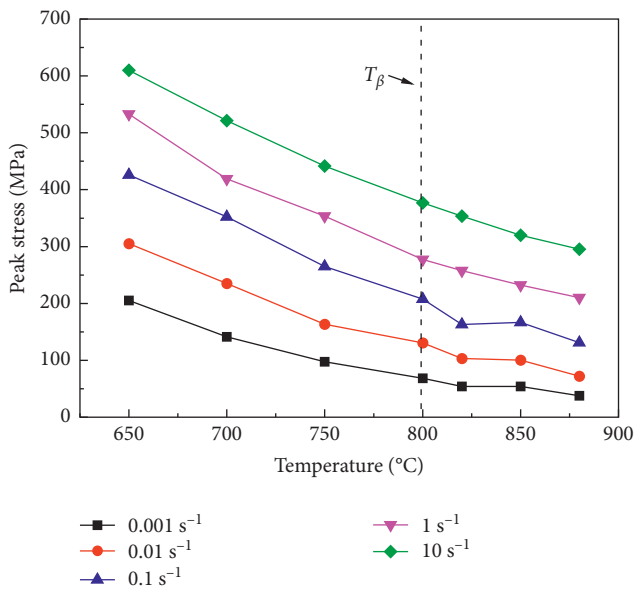

Figure 9: Flow softening behavior at different experiment conditions.

stress. This type of hot deformation behavior was also found in Ti-6554 [14] and Ti-5Al4Zr8Mo7V [18]. The deformed microstructures in Figures 10(a)~10(f) showed that recrystallization occurred on this occasion. When deformed in the $\alpha+\beta$ two-phase zone, little recrystallized grains were found at the junction of two or three grain boundaries, which indicated that dynamic recrystallization was hard to take place at lower temperature and lower strain rate, and the flow softening mechanism is dynamic recovery and dynamic recrystallization. When deformed in the β single-phase zone, small recrystallized grains distributed in the vicinity of the deformed grain boundaries, this type of recrystallization referred to as necklace recrystallization [7] was also observed in AZ31 [38], Ni-30 [39], and Ti55531 [16]. It can be concluded that at a higher temperature and lower strain rate, the dominant flow softening mechanism is dynamic recrystallization.

(2) Sharp initial peak stress followed by a softening effect to a steady-state is called discontinuous yielding phenomenon (DYP), which is presented with a strain rate of $0.1\sim1\,s^{-1}$ at all deformation temperatures. A similar phenomenon occurs in the other near β titanium alloys such as Ti-5553 [40] and Ti-1300 [41]. The deformed microstructures in Figures 10(g)~10(j) showed that dynamic recrystallization took place in the β single-phase zone, and flow localization bands were observed when deformed in the $\alpha+\beta$ two-phase zone. The occurrence of dynamic recrystallization reduced the dislocation density and eliminated the effect of strain hardening [42].

(3) At a strain rate of $10\,s^{-1}$, the flow curves reveal a continuous flow softening behavior below the transus temperature, and a discontinuous yielding phenomenon above the transus temperature. As can be seen in Figures 10(k)~10(l), the deformed microstructure showed that the flow instability was referred to as the occurrence of flow localization by

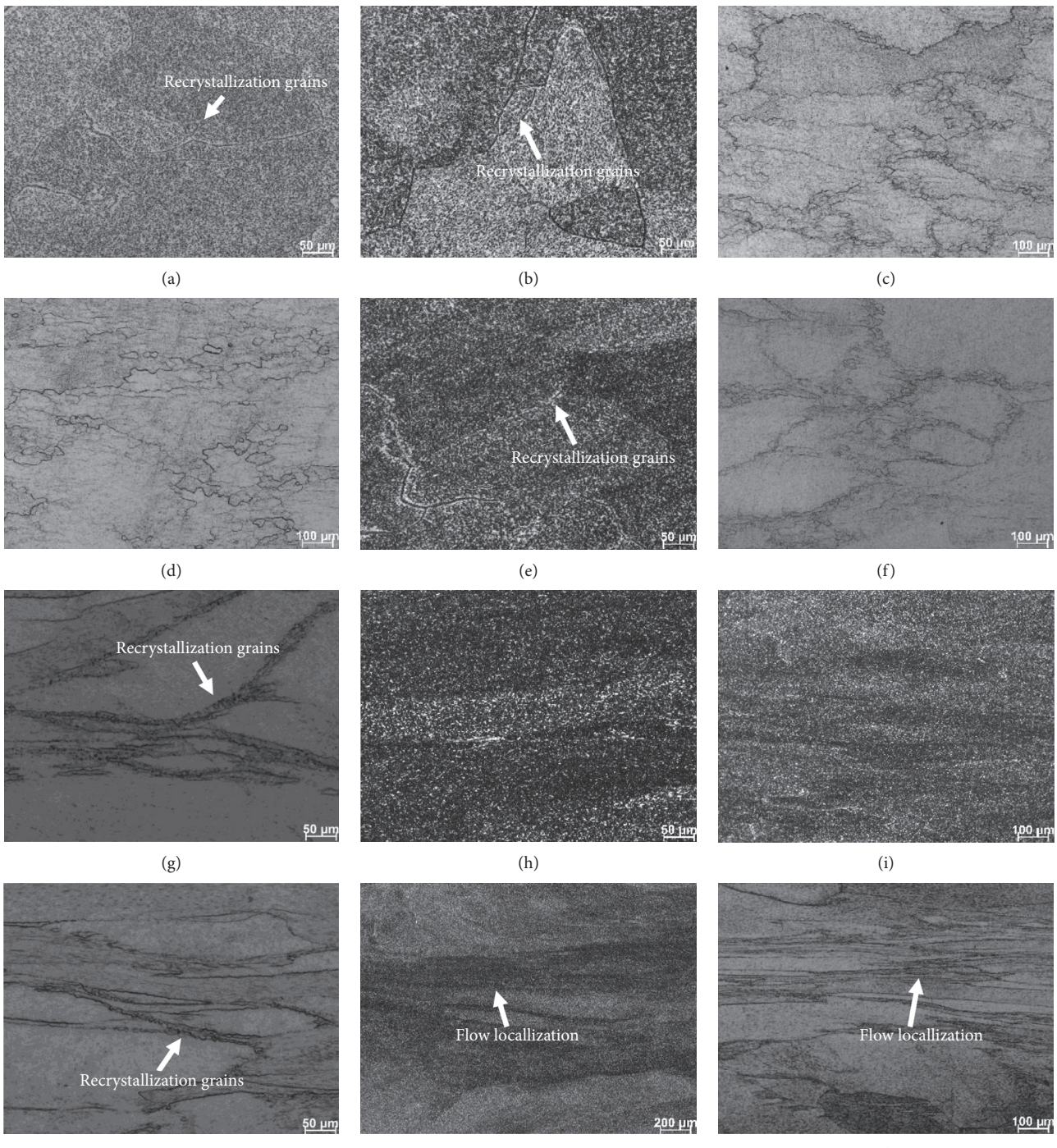

Figure 10: Deformed microstructure of TB18 alloy: (a) 700°C/0.001 s^{-1}; (b) 750°C/0.001 s^{-1}; (c) 800°C/0.001 s^{-1}; (d) 850°C/0.001 s^{-1}; (e) 700°C/0.01 s^{-1}; (f) 850°C/0.01 s^{-1}; (g) 850°C/0.1 s^{-1}; (h) 650°C/1 s^{-1}; (i) 700°C/1 s^{-1}; (j) 850°C/1 s^{-1}; (k) 750°C/10 s^{-1}; (l) 850°C/10 s^{-1}.

adiabatic heat, which is consistent with Ti-55531 [43].

3.2. Constitutive Relationship. The constitutive relationship can be established by the Arrhenius type, which is listed from equations (8) to (10). Taking the nature logarithm of equations (8) and (9), gives the following:

$$\ln \dot{\varepsilon} = n_1 \ln \sigma + \ln A_1 - \frac{Q}{RT} \text{ (for low stress level)}, \quad (11)$$

$$\ln \dot{\varepsilon} = \beta\sigma + \ln A_2 - \frac{Q}{RT} \text{ (for high stress level)}. \quad (12)$$

At the low stress level, the n_1 value can be obtained by plotting $\ln \sigma \sim \ln \dot{\varepsilon}$ at fixed temperatures and the slope of the

$\ln \sigma \sim \ln \dot{\varepsilon}$ gives the value n_1. At the high stress level, the β value can be calculated by plotting $\sigma \sim \ln \dot{\varepsilon}$ at given temperatures and the slope of the σ-$\ln \dot{\varepsilon}$ gives the β value.

The corrected flow stress and the corresponding strain rate (0.4) were then substituted into equations (11) and (12). The relationship between flow stress and strain rates is shown in Figure 11. The average slopes of the lines are used to compute the values of n_1 and β, which are 5.57391 and 0.03144 MPa^{-1}, respectively. Then, $\alpha = \beta/n_1 = 0.00564\ \text{MPa}^{-1}$.

For all stress levels, equation (10) can be represented as the following:

$$\dot{\varepsilon} = A[\sinh(\alpha\sigma)]^n \exp\left(-\frac{Q}{RT}\right). \tag{13}$$

Differentiating equation (12) gives the following:

$$Q = R\left\{\frac{\partial \ln \dot{\varepsilon}}{\partial \ln[\sinh(\alpha\sigma)]}\right\}_T \left\{\frac{\partial \ln[\sinh(\alpha\sigma)]}{\partial(1/T)}\right\}_{\dot{\varepsilon}}. \tag{14}$$

From equation (14), the Q value can be derived from the slopes of $\ln[\sinh(\alpha\sigma)]$-$\ln \dot{\varepsilon}$ and $\ln[\sinh(\alpha\sigma)]$-$1/T$. Substituting the values of the corrected flow stress, deformation temperature and corresponding strain rate at the strain of 0.4 into equation (14). Then, the relationships of $\ln \dot{\varepsilon}$-$\ln[\sinh(\alpha\sigma)]$ and $\ln[\sinh(\alpha\sigma)]$-$1000/T$ can be acquired, as shown in Figure 12. Because the slopes of the lines are approximately the same, the average slopes are used for acquiring the value of activated energy and it is 238.465 kJ/mol.

Taking the natural logarithm of both sides of equation (10) gives

$$\ln[\sinh(\alpha\sigma)] = \frac{\ln \dot{\varepsilon}}{n} + \frac{Q}{nRT} - \frac{\ln A}{n}. \tag{15}$$

The values of $((Q/nRT) - (\ln A/n))$ and $1/n$ are the intercept and slope of $\ln[\sinh(\alpha\sigma)] \sim \ln \dot{\varepsilon}$ plot, respectively. Substituting the value of Q, n, R, and T into equation (15), the values of $\ln A$ at different deformation temperatures can be obtained, the average of which is 23.89918.

According to this method, all the material constants with the strain range from 0.1 to 0.9 can be obtained as listed in Table 2.

3.3. Establishment and Verification of Constitutive Relationship. In equation (10), the influence of strain on high temperature deformation behavior is not considered. In order to consider the effect of strain, the material constants in constitutive equations (i.e., n, α, β, Q, and A) are expressed as polynomial functions of strain. First, the values of material constants (i.e., n, α, β, Q, and A) are calculated at various strain conditions; second, these values are fitted by polynomial function by the order from 2 to 9. Finally, a six-order polynomial is confirmed with a good correlation for TB18 alloy, as shown in the following equation and Figure 13:

$$\begin{aligned}
\alpha &= B_0 + B_1\varepsilon + B_2\varepsilon^2 + B_3\varepsilon^3 + B_4\varepsilon^4 + B_5\varepsilon^5 + B_6\varepsilon^6,\\
n &= C_0 + C_1\varepsilon + C_2\varepsilon^2 + C_3\varepsilon^3 + C_4\varepsilon^4 + C_5\varepsilon^5 + C_6\varepsilon^6,\\
Q &= D_0 + D_1\varepsilon + D_2\varepsilon^2 + D_3\varepsilon^3 + D_4\varepsilon^4 + D_5\varepsilon^5 + D_6\varepsilon^6,\\
\ln A &= E_0 + E_1\varepsilon + E_2\varepsilon^2 + E_3\varepsilon^3 + E_4\varepsilon^4 + E_5\varepsilon^5 + E_6\varepsilon^6.
\end{aligned} \tag{16}$$

After the materials constants are obtained, the flow stress at a constant strain can be predicted. The flow stress can be expressed as the function of the Zener–Hollomon parameters. And the proposed constitutive model can be summarized as follows:

$$\begin{aligned}
\sigma &= \frac{1}{\alpha}\ln\left\{\left(\frac{Z}{A}\right)^{1/n} + \left[\left(\frac{Z}{A}\right)^{2/n} + 1\right]^{1/2}\right\},\\
Z &= \dot{\varepsilon}\exp\left(\frac{Q}{RT}\right),\\
\alpha &= 0.006 - 0.013\varepsilon + 0.074\varepsilon^2 - 0.195\varepsilon^3 + 0.306\varepsilon^4\\
&\quad - 0.262\varepsilon^5 0.093\varepsilon^6,\\
n &= 4.186 - 2.798\varepsilon + 11.767\varepsilon^2 - 19.656\varepsilon^3 + 19.658\varepsilon^4\\
&\quad - 14.214\varepsilon^5 + 5.992\varepsilon^6,\\
Q &= 181.5 + 1702.78\varepsilon - 10879.25\varepsilon^2 + 31126\varepsilon^3 - 46483\varepsilon^4\\
&\quad + 35064.882\varepsilon^5 - 10533.241\varepsilon^6,\\
\ln A &= 17.03 + 200.735\varepsilon - 1274.8\varepsilon^2 + 3633.545\varepsilon^3 - 5414.6\varepsilon^4\\
&\quad + 4084.5\varepsilon^5 - 1229.6\varepsilon^6.
\end{aligned} \tag{17}$$

The comparison between the corrected flow stress and the predicted data from the strain-compensated constitutive equation at different deformation temperatures and strain rates are shown in Figure 14. It can be seen that the predicted flow stress matches well with the corrected results at different deformation conditions.

In order to quantify the accuracy of the constitutive equation, standard statistical parameters, namely, correlation coefficient (R) and average absolute relative error (AARE) are used [44], which are expressed as follows:

$$\begin{aligned}
R &= \frac{\sum_{i=1}^{n}(E_i - \overline{E})(P_i - \overline{P})}{\sqrt{\sum_{i=1}^{n}(E_i - \overline{E})^2 \sum_{i=1}^{n}(P_i - \overline{P})^2}},\\
\text{AARE}(\%) &= \frac{1}{n}\sum_{i=1}^{n}\left|\frac{E_i - P_i}{E_i}\right| \times 100,
\end{aligned} \tag{18}$$

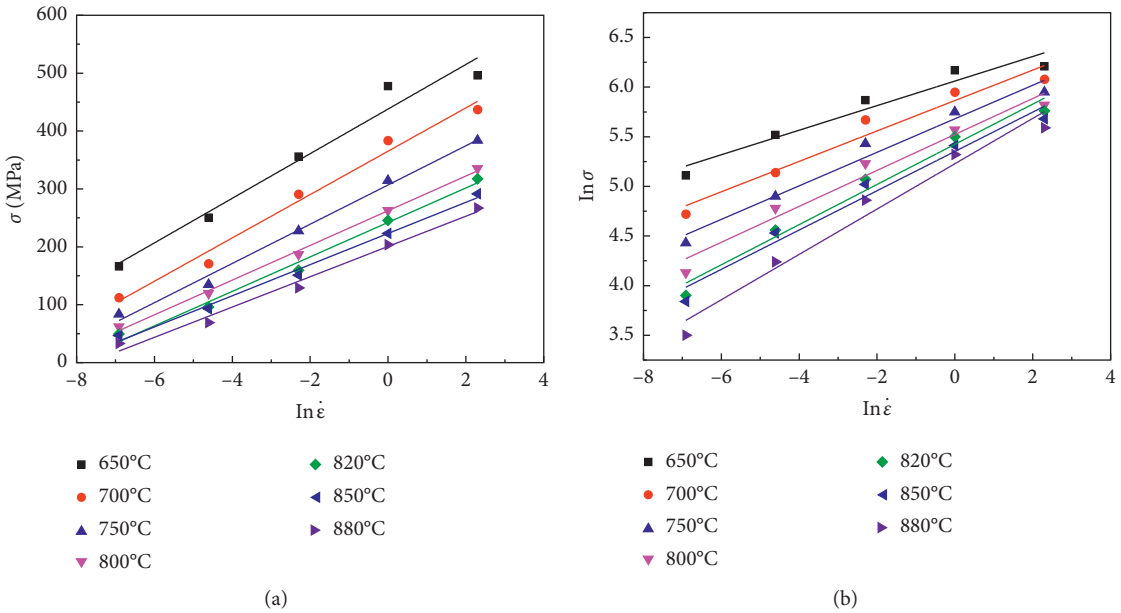

Figure 11: Relationship between (a) σ~$\ln \dot{\varepsilon}$ and (b) $\ln \sigma \sim \ln \dot{\varepsilon}$.

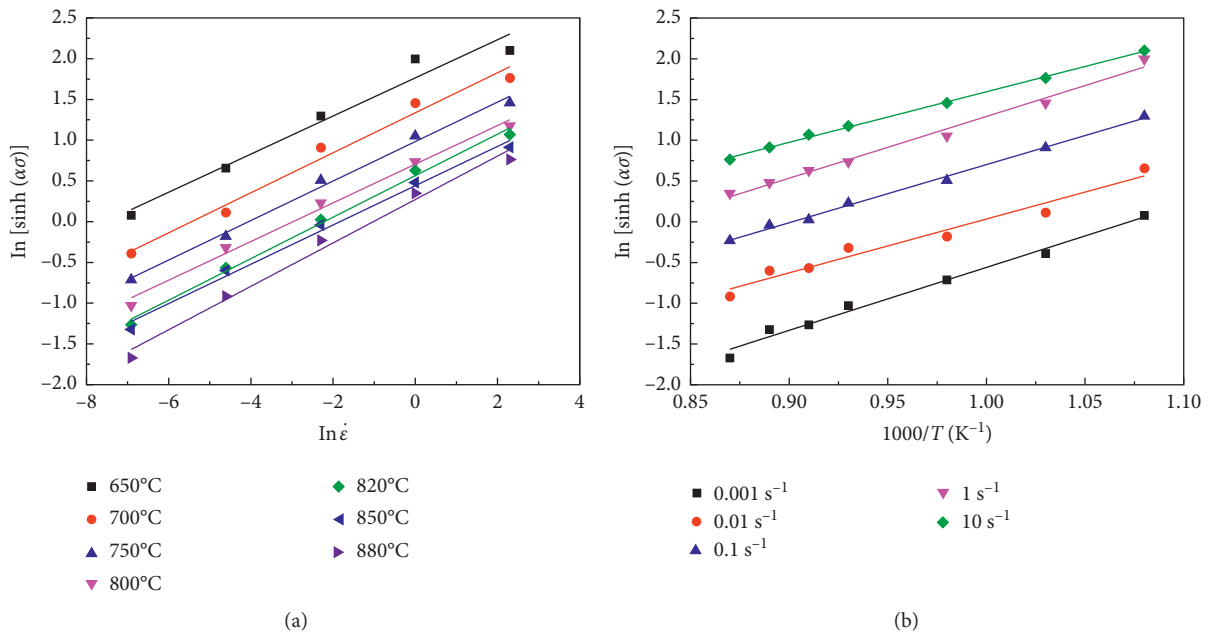

Figure 12: Relationship between (a) $\ln[\sinh(\alpha\sigma)]$-$\ln \dot{\varepsilon}$, (b) $\ln[\sinh(\alpha\sigma)]$-1000/(T).

Table 2: Material constants and m, Q values at different true strains.

True strain	n	α	$\ln A$	Q (kJ/mol)
0.1	4.00701	0.00516	27.49874	269.882
0.2	3.96643	0.00513	27.76949	271.675
0.3	4.01222	0.00531	25.93519	255.724
0.4	4.06849	0.00564	23.89918	238.465
0.5	4.16015	0.00595	23.02189	230.871
0.6	4.22272	0.00621	21.90254	220.727
0.7	4.2919	0.00651	20.92657	212.121
0.8	4.38679	0.00668	20.39894	207.074
0.9	4.56564	0.00706	19.8164	202.771

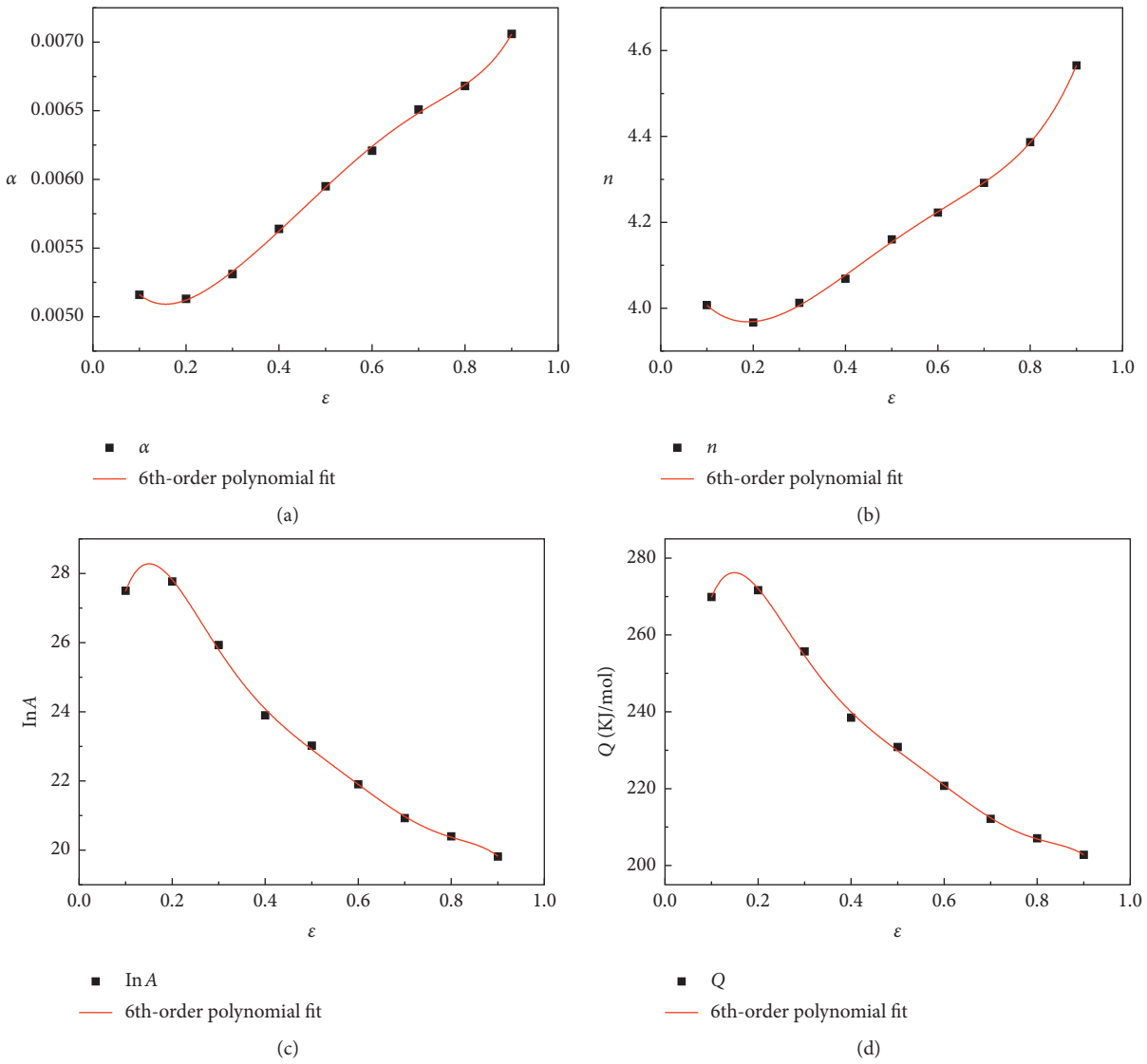

Figure 13: Polynomial fit of (a) α, (b) n, (c) ln A, and (d) Q at different true strains.

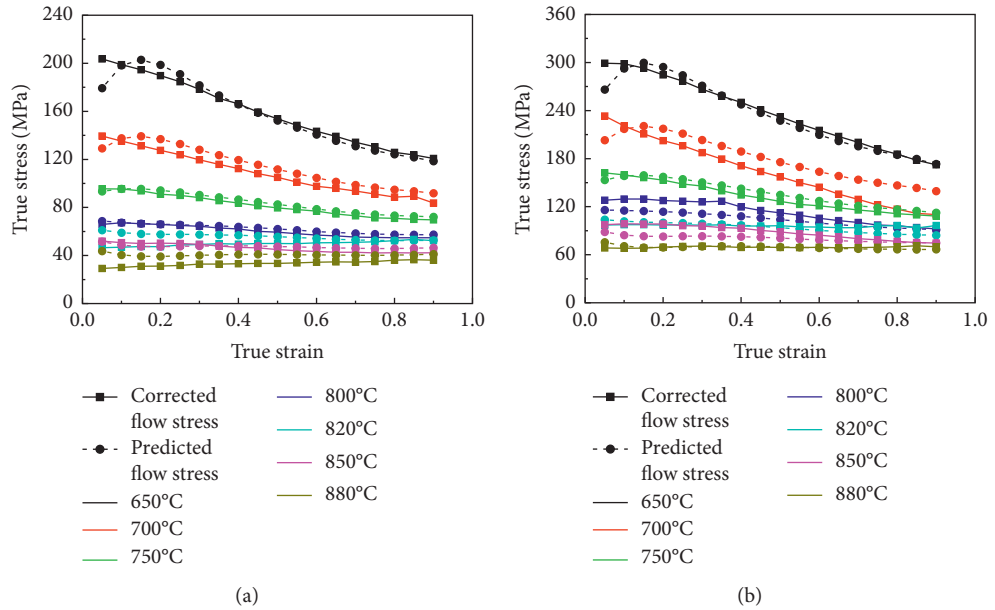

Figure 14: Continued.

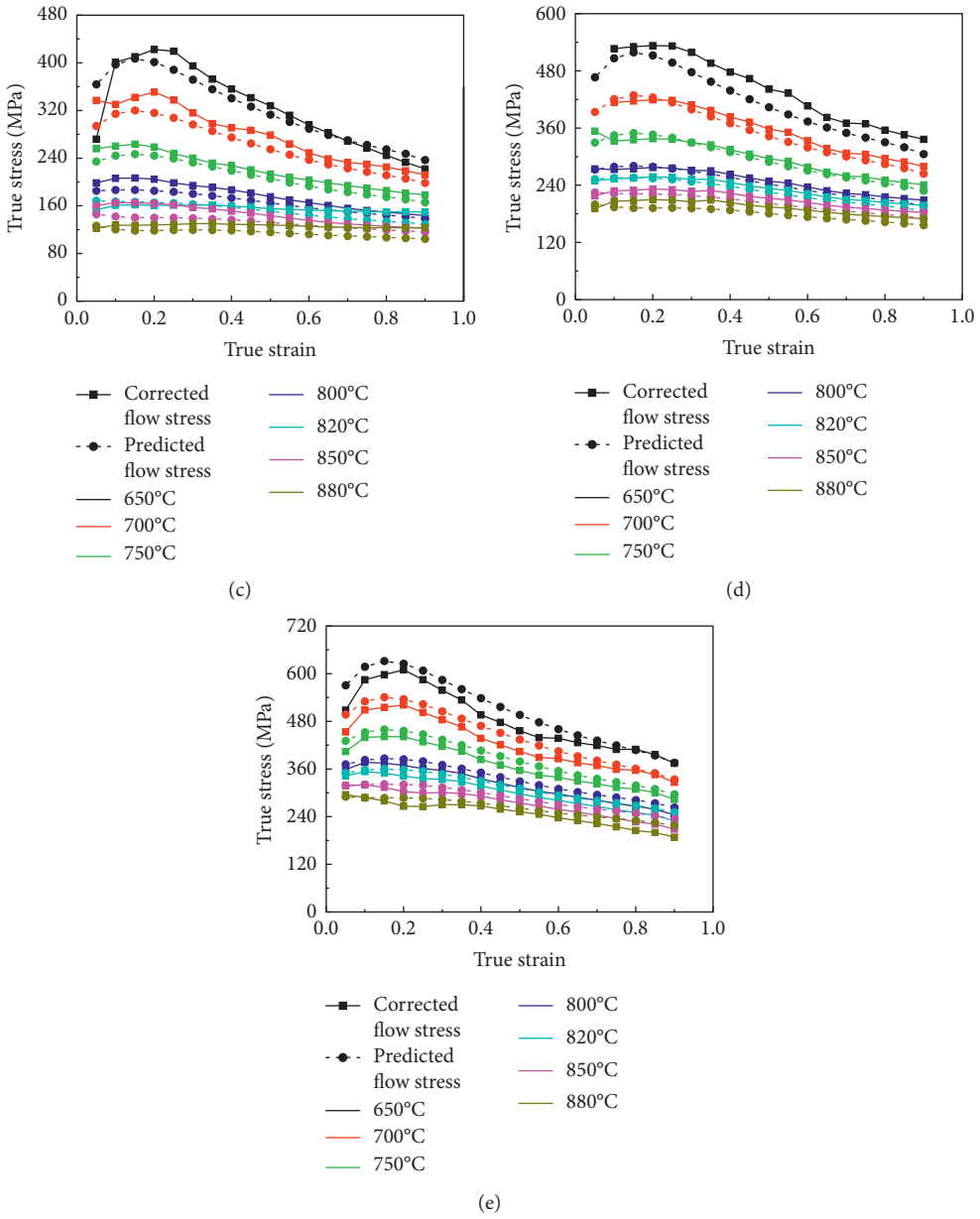

FIGURE 14: Comparison between the corrected and the predicted (considering the compensation of strain) flow stress curves: (a) 0.001 s^{-1}, (b) 0.01 s^{-1}, (c) 0.1 s^{-1}, (d) 1 s^{-1}, and (e) 10 s^{-1}.

where E is the original value and P is the predicted one obtained from the constitutive equation, $\overline{E}$ and $\overline{P}$ represent the mean values of E and P, respectively. N is the total number of data points. The correlation coefficient is a commonly used statistic, which reflects the strength of the linear relationship between observed data and predicted data by comparing relative errors term by term. A good correlation ($R = 99.2\%$) is obtained between the original and the predicted data, as seen in Figure 15. The calculated AARE value equals to 6.1% at the tested deformation conditions. The statistical results show high accuracy of the established constitutive equation for the TB18 alloy ranging from the strain rate of 0.001~10 s^{-1} and the temperature of 650~880°C.

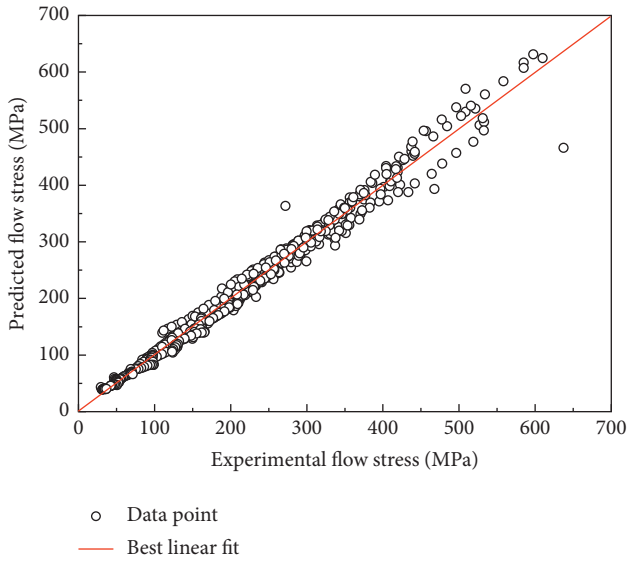

FIGURE 15: Comparison between the experimental and predicted flow stress data.

4. Conclusions

In this work, the isothermal hot compression test with a temperature of 650–880°C and a strain rate of 0.001~10 s^{-1} was performed to study the hot deformation behavior of TB18 alloy. The following conclusions could be drawn from the current research:

(1) The measured flow stress was revised by friction and temperature correction, and the peak stress decreased with the deformation temperature increase and the strain rate decline.

(2) The flow stress curves revealed three typical characteristics at various deformation conditions: (1) At lower strain rate of 0.001~0.01 s^{-1}, the flow stress continues to decrease as the strain rate increases after the flow stress reaches the peak stress. The flow softening mechanism is dynamic recovery and dynamic recrystallization at lower temperatures and dynamic recrystallization at higher temperatures. (2) The discontinuous yielding phenomenon could be seen at a moderate strain rate of 1 s^{-1}, dynamic recrystallization took place in the β single-phase zone, and flow localization bands were observed in the $\alpha+\beta$ two-phase zone. (3) At a higher strain rate of 10 s^{-1}, the flow instabilities were referred to as the occurrence of flow localization by adiabatic heat.

(3) The constitutive equation considering the compensation of strain was established to predict the flow stress, whose results accurately showed the correlation coefficient and the AARE are 99.2% and 6.1%, respectively.

Data Availability

The flow stress data used to support the findings of this study are available from the corresponding author upon request.

Conflicts of Interest

The authors declare that there are no conflicts of interest regarding the publication of this paper.

References

[1] X. G. Fan, Y. Zhang, H. J. Zheng, Z. Q. Zhang, P. F. Gao, and M. Zhan, "Pre-processing related recrystallization behavior in β annealing of a near-β Ti-5Al-5Mo-5V-3Cr-1Zr titanium alloy," *Materials Characterization*, vol. 137, pp. 151–161, 2018.

[2] X. Xu, L.-M. Dong, H.-B. Ba, Z.-Q. Zhang, and R. Yang, "Hot deformation behavior and microstructural evolution of beta C titanium alloy in β phase field," *Transactions of Nonferrous Metals Society of China*, vol. 26, no. 11, pp. 2874–2882, 2016.

[3] J. Zhang and H. Di, "Deformation heating and flow localization in Ti-15-3 metastable β titanium alloy subjected to high Z deformation," *Materials Science and Engineering: A*, vol. 676, pp. 506–509, 2016.

[4] P. Manda, V. Singh, U. Chakkingal, and A. K. Singh, "Development of α precipitates in metastable Ti-5Al-5Mo-5V-3Cr and similar alloys," *Materials Characterization*, vol. 120, pp. 220–228, 2016.

[5] M. Jackson, R. Dashwood, H. Flower, and L. Christodoulou, "The microstructural evolution of near beta alloy Ti-10V-2Fe-3Al during subtransus forging," *Metallurgical and Materials Transactions A*, vol. 36, no. 5, pp. 1317–1327, 2005.

[6] S. Shekhar, R. Sarkar, S. K. Kar, and A. Bhattacharjee, "Effect of solution treatment and aging on microstructure and tensile properties of high strength β titanium alloy, Ti-5Al-5V-5Mo-3Cr," *Materials & Design*, vol. 66, pp. 596–610, 2015.

[7] I. Weiss and S. Semiatin, "Thermomechanical processing of beta titanium alloys—an overview," *Materials Science and Engineering: A*, vol. 243, no. 1-2, pp. 46–65, 1998.

[8] D. Samantaray, S. Mandal, and A. K. Bhaduri, "Constitutive analysis to predict high-temperature flow stress in modified 9Cr-1Mo (P91) steel," *Materials & Design*, vol. 31, no. 2, pp. 981–984, 2010.

[9] H. Shi, A. J. McLaren, C. M. Sellars, R. Shahani, and R. Bolingbroke, "Constitutive equations for high temperature flow stress of aluminium alloys," *Materials Science and Technology*, vol. 13, no. 3, pp. 210–216, 1997.

[10] V. G. Krishna, Y. V. R. K. Prasad, N. C. Birla, and G. S. Rao, "Processing map for the hot working of near-α titanium alloy 685," *Journal of Materials Processing Technology*, vol. 71, no. 3, pp. 377–383, 1997.

[11] S. L. Semiatin, V. Seetharaman, and I. Weiss, "The thermomechanical processing of alpha/beta titanium alloys," *JOM*, vol. 49, no. 6, pp. 33–39, 1997.

[12] L. Lei, X. Huang, M. Wang et al., "Effect of hot compressive deformation on the martensite transformation of Ti-10V-2Fe-3Al titanium alloy," *Materials Science and Engineering: A*, vol. 530, pp. 591–601, 2011.

[13] Y. C. Lin, J. Huang, H.-B. Li, and D.-D. Chen, "Phase transformation and constitutive models of a hot compressed TC18 titanium alloy in the $\alpha+\beta$ regime," *Vacuum*, vol. 157, pp. 83–91, 2018.

[14] S. Long, Y.-F. Xia, P. Wang et al., "Constitutive modelling, dynamic globularization behavior and processing map for Ti-6Cr-5Mo-5V-4Al alloy during hot deformation," *Journal of Alloys and Compounds*, vol. 796, pp. 65–76, 2019.

[15] J. Zhao, J. Zhong, F. Yan, F. Chai, and M. Dargusch, "Deformation behaviour and mechanisms during hot compression

at supertransus temperatures in Ti-10V-2Fe-3Al," *Journal of Alloys and Compounds*, vol. 710, pp. 616–627, 2017.

[16] W. Chuan and H. Liang, "Hot deformation and dynamic recrystallization of a near-beta titanium alloy in the β single phase region," *Vacuum*, vol. 156, pp. 384–401, 2018.

[17] J. K. Fan, H. C. Kou, M. J. Lai, B. Tang, H. Chang, and J. S. Li, "Characterization of hot deformation behavior of a new near beta titanium alloy: Ti-7333," *Materials & Design*, vol. 49, pp. 945–952, 2013.

[18] J. Lei, W. Zhu, L. Chen, Q. Sun, L. Xiao, and J. Sun, "Deformation behaviour and microstructural evolution during the hot compression of Ti-5Al4Zr8Mo7V alloy," *Materials Today Communications*, vol. 23, Article ID 100873, 2020.

[19] C. Zener and J. H. Hollomon, "Effect of strain rate upon plastic flow of steel," *Journal of Applied Physics*, vol. 15, no. 1, pp. 22–32, 1944.

[20] C. M. Sellars and W. J. McTegart, "On the mechanism of hot deformation," *Acta Metallurgica*, vol. 14, no. 9, pp. 1136–1138, 1966.

[21] J. J. Jonas, C. M. Sellars, and W. J. M. Tegart, "Strength and structure under hot-working conditions," *International Materials Reviews*, vol. 14, no. 1, pp. 1–24, 1969.

[22] F. A. Slooff, J. Zhou, J. Duszczyk, and L. Katgerman, "Constitutive analysis of wrought magnesium alloy Mg-Al4-Zn1," *Scripta Materialia*, vol. 57, no. 8, pp. 759–762, 2007.

[23] G. Ji, F. Li, Q. Li, H. Li, and Z. Li, "A comparative study on Arrhenius-type constitutive model and artificial neural network model to predict high-temperature deformation behaviour in Aermet100 steel," *Materials Science and Engineering: A*, vol. 528, no. 13-14, pp. 4774–4782, 2011.

[24] W. Peng, W. Zeng, Q. Wang, and H. Yu, "Comparative study on constitutive relationship of as-cast Ti60 titanium alloy during hot deformation based on Arrhenius-type and artificial neural network models," *Materials & Design*, vol. 51, pp. 95–104, 2013.

[25] C. Gang, C. Wei, M. Li et al., "Strain-compensated arrhenius-type constitutive model for flow behavior of Al-12Zn-2.4Mg-1.2Cu alloy," *Rare Metal Materials and Engineering*, vol. 44, no. 9, pp. 2120–2125, 2015.

[26] Z. Cai, F. Chen, and J. Guo, "Constitutive model for elevated temperature flow stress of AZ41M magnesium alloy considering the compensation of strain," *Journal of Alloys and Compounds*, vol. 648, pp. 215–222, 2015.

[27] Y. C. Lin, Y.-C. Xia, X.-M. Chen, and M.-S. Chen, "Constitutive descriptions for hot compressed 2124-T851 aluminum alloy over a wide range of temperature and strain rate," *Computational Materials Science*, vol. 50, no. 1, pp. 227–233, 2010.

[28] B. Roebuck, J. D. Lord, M. Brooks, M. S. Loveday, C. M. Sellars, and R. W. Evans, "Measurement of flow stress in hot axisymmetric compression tests," *Materials at High Temperatures*, vol. 23, no. 2, pp. 59–83, 2006.

[29] R. Ebrahimi and A. Najafizadeh, "A new method for evaluation of friction in bulk metal forming," *Journal of Materials Processing Technology*, vol. 152, no. 2, pp. 136–143, 2004.

[30] L. Li, J. Zhou, and J. Duszczyk, "Determination of a constitutive relationship for AZ31B magnesium alloy and validation through comparison between simulated and real extrusion," *Journal of Materials Processing Technology*, vol. 172, no. 3, pp. 372–380, 2006.

[31] Z. Wan, L. Hu, Y. Sun, T. Wang, and Z. Li, "Hot deformation behavior and processing workability of a Ni-based alloy," *Journal of Alloys and Compounds*, vol. 769, pp. 367–375, 2018.

[32] P. Dadras and J. F. Thomas, "Characterization and modeling for forging deformation of Ti-6Ai-2Sn-4Zr-2Mo-0.1 Si," *Metallurgical Transactions A*, vol. 12, no. 11, pp. 1867–1876, 1981.

[33] R. L. Goetz and S. L. Semiatin, "The adiabatic correction factor for deformation heating during the uniaxial compression test," *Journal of Materials Engineering and Performance*, vol. 10, no. 6, pp. 710–717, 2001.

[34] J. H. Kim, S. L. Semiatin, and C. S. Lee, "Constitutive analysis of the high-temperature deformation of Ti-6Al-4V with a transformed microstructure," *Acta Materialia*, vol. 51, no. 18, pp. 5613–5626, 2003.

[35] H.-Y. Wu, J.-C. Yang, F.-J. Zhu, and C.-T. Wu, "Hot compressive flow stress modeling of homogenized AZ61 Mg alloy using strain-dependent constitutive equations," *Materials Science and Engineering: A*, vol. 574, pp. 17–24, 2013.

[36] H. McQueen and N. Ryan, "Constitutive analysis in hot working," *Materials Science and Engineering: A*, vol. 322, no. 1-2, pp. 43–63, 2002.

[37] L. Tan, Y. Li, G. He, F. Liu, Y. Nie, and L. Jiang, "Optimized hot workability of a powder metallurgy nickel-base superalloy," *Materials Characterization*, vol. 147, pp. 340–352, 2019.

[38] W. X. Wu, L. Jin, J. Dong, Z. Y. Zhang, and W. J. Ding, "Effect of initial microstructure on the dynamic recrystallization behavior of Mg-Gd-Y-Zr alloy," *Materials Science and Engineering: A*, vol. 556, pp. 519–525, 2012.

[39] H. Beladi, P. Cizek, and P. D. Hodgson, "Dynamic recrystallization of austenite in Ni-30 Pct Fe model alloy: microstructure and texture evolution," *Metallurgical and Materials Transactions A*, vol. 40, no. 5, pp. 1175–1189, 2009.

[40] N. G. Jones, R. J. Dashwood, D. Dye, and M. Jackson, "The flow behavior and microstructural evolution of Ti-5Al-5Mo-5V-3Cr during subtransus isothermal forging," *Metallurgical and Materials Transactions A*, vol. 40, no. 8, pp. 1944–1954, 2009.

[41] H. Z. Zhao, L. Xiao, P. Ge, J. Sun, and Z. P. Xi, "Hot deformation behavior and processing maps of Ti-1300 alloy," *Materials Science and Engineering: A*, vol. 604, pp. 111–116, 2014.

[42] B. Han and Z. Xu, "Microstructural evolution of Fe–32% Ni alloy during large strain multi-axial forging," *Materials Science and Engineering: A*, vol. 447, no. 1-2, pp. 119–124, 2007.

[43] M. Dikovits, C. Poletti, and F. Warchomicka, "Deformation mechanisms in the near-β titanium alloy Ti-55531," *Metallurgical and Materials Transactions A*, vol. 45, no. 3, pp. 1586–1596, 2014.

[44] S. Mandal, V. Rakesh, P. V. Sivaprasad, S. Venugopal, and K. V. Kasiviswanathan, "Constitutive equations to predict high temperature flow stress in a Ti-modified austenitic stainless steel," *Materials Science and Engineering: A*, vol. 500, no. 1-2, pp. 114–121, 2009.